FDTD Microcavity Simulations: Design and Experimental Realization of Waveguide-Coupled Single-Mode Ring and Whispering-Gallery-Mode Disk Resonators

S. C. Hagness, *Student Member, IEEE,* D. Rafizadeh, *Student Member, IEEE,*
S. T. Ho, *Member, IEEE,* and A. Taflove, *Fellow, IEEE*

Abstract—**We investigate the properties of high-Q, wide free-spectral-range semiconductor microcavity ring and disk resonators coupled to submicron-width waveguides. Key optical design parameters are characterized using finite-difference time-domain (FDTD) solutions of the full-wave Maxwell's equations. We report coupling efficiencies and resonant frequencies that include the effects of waveguide dispersion and bending and scattering losses. For diameters of 5 μm, the microcavity resonators can have Q's in the several thousands and a free spectral range of 6 THz (50 nm) in the 1.55 μm, wavelength range. Studies of the transmittance characteristics illustrate the transition from single-mode resonances to whispering-gallery-mode resonances as the waveguide width of the microring is increased to form a solid microdisk. We present nanofabrication results and experimentally measured transmission resonances of AlGaAs/GaAs microcavity resonators designed in part with this method.**

Index Terms— **FDTD methods, integrated optics, microresonators, numerical analysis, optical device fabrication.**

I. Introduction

OPTICAL ring and disk resonators are useful components for wavelength filtering, routing, switching, modulation, and multiplexing/demultiplexing applications [1]–[4]. The ideal resonator for wavelength division multiplexing (WDM) systems has a wide free spectral range (FSR) and high finesse to accommodate many channels, high transmission at resonance to minimize insertion loss, and a large extinction ratio to minimize crosstalk [5]. Ring resonators based on waveguide structures with weak lateral confinement have very low propagation loss [6], [7]; however, the small refractive index contrast of the weakly guiding structures leads to high radiative bending losses at ring/disk diameters below 1 mm. Therefore, the FSR, which is inversely proportional to the diameter, has been limited to 26 GHz (0.15 nm at 1.3 μm) [8] for a single ring and 100 GHz (0.8 nm at 1.55 μm) [9] for a double ring resonator. Various techniques have been reported for increasing the FSR without decreasing the diameter, including a triple-coupler ring resonator that offers twice the FSR of the double ring resonator with the same radius of curvature [10].

More recently, high-index-contrast semiconductor ring and disk resonators have attracted much attention. By etching down through the guiding layer, strong lateral confinement is achieved, thus allowing diameters below 1 mm with negligible bending losses. The advantages of these compact strongly guiding resonators include large longitudinal mode spacing and the potential for high-density integration with other semiconductor devices. For active devices, the wide FSR can yield single-mode operation above threshold. Several groups have demonstrated strongly guiding semiconductor ring lasers [11]–[14] with diameters in the range from 10 to 500 μm and large waveguide widths from 4 to 20 μm. To obtain light output, these ring resonators are coupled to output guides via Y junctions because directional couplers for strongly guiding waveguides require very small gaps; the low finesse that results from such strong output coupling is compensated by high gain in these active devices. Semiconductor microdisk lasers [15]–[20] with diameters less than 20 μm and high-Q modes have also been demonstrated. However, directional output is difficult to obtain from the isolated disks [21], [22].

Nanofabrication techniques now allow the realization of semiconductor microcavity ring and disk resonators with evanescent wave coupling to submicron-width waveguides across submicron-width air gaps, as proposed recently [23], [24]. Microcavity resonators based on semiconductor waveguides with a very large lateral refractive index contrast (air-semiconductor-air) can have diameters as small as 1–2 μm with negligible bending loss [25]. With diameters as small as 5 μm, the FSR can be as wide as 6 THz (50 nm). For example, this FSR is wide enough to accomodate a set of WDM channels across the 30-nm erbium amplifier bandwidth. Thus, microcavity ring and disk resonators offer FSR's that are more than an order-of-magnitude wider than those previously achieved with larger weakly guiding ring resonators. With high-quality etching, the scattering losses can be kept low enough to achieve simultaneously a high finesse. Additionally, these resonators can be integrated with low-threshold photonic-wire microcavity lasers [26]. Potential applications of the passive resonators include micron-size

Manuscript received April 21, 1997; revised August 4, 1997. This work was supported by AFOSR/ARPA under Contract F49620-96-1-0262, under NSF Grant ECS-9218494, and by Cray Research, Inc. The work of S. C. Hagness was supported in part by an NSF Graduate Fellowship.

The authors are with the Department of Electrical and Computer Engineering, McCormick School of Engineering, Northwestern University, Evanston, IL 60208 USA.

Publisher Item Identifier S 0733-8724(97)08131-0.

channel-dropping filters [27], frequency-domain switches, and intensity/phase modulators.

In this paper, we present results from rigorous finite-difference time-domain numerical simulations used to characterize key optical design parameters of high-index-contrast microcavity ring and disk resonators coupled to single-mode or nearly single-mode waveguides. First, we describe the computational method for modeling the resonators. Second, we present studies of the input/output coupling efficiencies, followed by studies of the resonance behavior of single-mode microrings and whispering-gallery mode microdisks. Finally, we discuss the design of actual device prototypes and present nanofabrication and experimental results.

II. The FDTD Method

Ring and disk resonators at microwave and optical frequencies have been subject to a variety of analytical and numerical methods. Examples include the analysis of the coupling efficiencies, resonant frequencies, and bending losses of larger-scale low-index-contrast ring and disk resonators at optical frequencies [25], [28]–[31]. At microwave frequencies, the resonance behavior of high-index-contrast dielectric disks coupled to straight waveguides has been analyzed [32]. Several approximate models have been used to estimate the resonant frequencies of isolated semiconductor microdisks with ideally smooth edges [33], [34].

This paper applies the full-wave finite-difference time-domain (FDTD) method of solving Maxwell's equations [35], [36] to the analysis of high-index-contrast waveguide-coupled microcavity ring and disk resonators. The rationale for this approach is that FDTD has been extensively applied to design complicated RF and microwave devices with dimensions comparable to the radiation wavelength. As the size of photonic and optoelectronic components approaches that of the optical wavelength, FDTD modeling has the potential to play a similarly useful design role. For example, this method has been used to analyze the whispering-gallery modes of isolated microdisks on pedestals [37] or suspended in air [38]. FDTD simulations of isolated idealized microdisks have been used as baselines for comparison with analytical mode calculations [39]. Simulations have also been performed to highlight the potential of microring and disk resonators side-coupled to an optical signal bus [27].

The accuracy of the FDTD method for problems in linear optics was first demonstrated for the directional coupler [40]. Since then, the perfectly matched layer (PML) absorbing boundary condition (ABC) has been introduced [41]. The PML ABC provides effective reflection coefficients due to grid truncation as low as 1/3000th those of standard ABC's; essentially, two- and three-dimensional (2-D and 3-D) FDTD grids can be terminated without reflection [42]. The improved performance of the PML ABC relative to any earlier technique has provided the increased dynamic range required for sensitive numerical simulations such as the analysis of antireflection coatings [43]. The importance of the PML for modeling highly dispersive optical waveguides is in the termination of waveguides extending beyond the FDTD grid boundaries. Reuter *et al.* [44] demonstrated that multimodal and dispersive waveguiding structures extending beyond the edges of the conventional FDTD grid can be terminated accurately by the PML, with reflection coefficients less than -75 dB, for a wide range of group velocities.

Because of the importance of accurate modeling of relatively large waveguide dispersion (discussed in the following section), we briefly review the accuracy of FDTD for modeling propagating waveguide modes. Consider a two-dimensional (2-D) problem where the z-directed electric field is normal to the x-y plane of the grid. For a linear nondispersive material of infinite extent in the z-direction, Maxwell's equations for the electric and magnetic fields, E_z, H_x, and H_y are given by

$$\frac{\partial H_x}{\partial t} = -\frac{1}{\mu_o}\frac{\partial E_z}{\partial y}, \quad \frac{\partial H_y}{\partial t} = \frac{1}{\mu_o}\frac{\partial E_z}{\partial x} \tag{1}$$

$$\frac{\partial E_z}{\partial t} = \frac{1}{\epsilon}\left[\frac{\partial H_y}{\partial x} - \frac{\partial H_x}{\partial y} - \sigma E_z\right]. \tag{2}$$

Using the FDTD method to solve (1) and (2), we compute the longitudinal propagation constant β for a lossless, strongly guiding planar waveguide consisting of a 0.3-μm-wide core ($n = 3.2$) surrounded by air ($n = 1$). A fundamental mode is sourced at one end of the waveguide. The excitation is a 20-fs Gaussian pulse modulating a carrier of 200 THz. The pulse width is chosen to cover the frequency range of interest, so that the frequency characteristics of β can be obtained in a single run. We record E_z as the pulsed waveguide mode propagates past two observation points located along the center of the core at the opposite end of the waveguide. By taking the ratio of the discrete Fourier transforms (DFT's) of the pulse at these two points, β is computed over the pulse's full bandwidth. Comparison of the FDTD-computed β versus ν with the known dispersion relation [45] indicates a difference of less than than 2 parts per thousand for a grid resolution of 13.6 nm. Similar accuracy is obtained for the group velocity.

III. Microcavity Ring and Disk Resonator Design

Mechanisms which can affect the Q of microcavity ring resonators are intrinsic material absorption, radiation loss caused by waveguide bending and surface roughness scattering, and coupling from the cavity to the adjacent waveguides. The focus of the experimental work presented in this paper is on passive devices for which the absorption loss is negligible. Bending losses are inherently included in any FDTD model of curved waveguides. Strong lateral confinement is achieved in the semiconductor waveguides by etching down through the lower cladding layer, resulting in sidewall roughness. Analytical estimates of the surface-roughness loss indicate that scattering in microcavities can not only limit the Q of these devices [39], but also lead to backreflections into the counterpropagating mode [46]. To simulate the side-wall roughness that causes scattering losses, we use a stepped-edge approximation to the ideally smooth circular geometries. The side-wall corrugation in our models is approximately 14 nm, about 1/40 of the optical wavelength within the material of the waveguide core. In addition to resolving the side-wall roughness which has been experimentally observed to be on the order from 10 to

20 nm, this grid cell size is sufficient to maintain extremely high numerical accuracy. The flexibility of the FDTD method allows us to quantify the coupling efficiencies for arbitrarily shaped input/output waveguides.

The submicron width and large lateral index contrast of the semiconductor waveguides leads to significant optical waveguide dispersion. The impact of this is illustrated with the following equation for the free spectral range between the mth and $(m+1)$th longitudinal modes:

$$\Delta\nu_{\mathrm{FSR}} = \frac{c}{\pi}\left\{\frac{m+1}{d_{\mathrm{eff}}(\nu_{m+1})n_{\mathrm{eff}}(\nu_{m+1})} - \frac{m}{d_{\mathrm{eff}}(\nu_m)n_{\mathrm{eff}}(\nu_m)}\right\} \tag{3}$$

where n_{eff} is the effective index of the waveguide mode and d_{eff} is the effective disk/ring diameter of the microring or disk. The quantity πd_{eff} corresponds to the circumferential path traveled by the peak of the guided mode; that is, d_{eff} is the distance between the two peaks of the transverse mode profile found along the ring/disk diameter. For a resonator with a relatively large diameter, d, and negligible waveguide dispersion, (3) is commonly simplified to $\Delta\nu_{\mathrm{FSR}} = c/d\pi n_{\mathrm{eff}}$. However, for semiconductor microcavity ring and disk resonators, $n_{\mathrm{eff}}(\nu_m) \neq n_{\mathrm{eff}}(\nu_{m+1})$ because the waveguide dispersion is strong and the longitudinal mode spacing is so wide. Also, d_{eff} is significantly smaller than the diameter d and is a function of frequency. Therefore, (3) cannot be simplified further for the case of semiconductor microcavity resonators. Likewise, the Q is affected by the relatively large dispersion [47].

The waveguide structure in the vertical direction consists of a 0.45-μm-thick GaAs guiding layer with AlGaAs cladding layers above and below. This structure is weakly guiding in the vertical direction in order to allow for input coupling of light from an external fiber or planar-emitting device. In our 2-D simulations, we account for the vertical waveguide thickness and material composition by using the effective refractive index for the fundamental mode at $\lambda = 1.5\,\mu$m as the material index of the core in the 2-D simulations. In the horizontal direction (the plane of the FDTD grid), the waveguide core is bordered by air. With $n_{\mathrm{core}} = 3.2$ and $n_{\mathrm{cladding}} = 1.0$, the waveguides have strong lateral confinement.

IV. Coupling Efficiencies for Microcavity Ring Resonators

A. Microrings Coupled to Straight Waveguides

Fig. 1 shows a typical geometry of a microcavity ring/disk resonator. The two tangential straight waveguides (WG1 and WG2) serve as evanescent wave input and output couplers. The coupling efficiency between the waveguides and the ring/disk is controlled by the size, g, of the air gap, and the ring/disk outer diameter, d, which affects the coupling interaction length. We accordingly investigate the coupling efficiency of the microcavity ring resonator structure of Fig. 1 by varying g and d. In these simulations, the width of WG1, WG2, and the microring waveguide is 0.3 μm. For this width, the straight waveguides support only one symmetric and one antisymmetric mode at $\lambda = 1.5\,\mu$m.

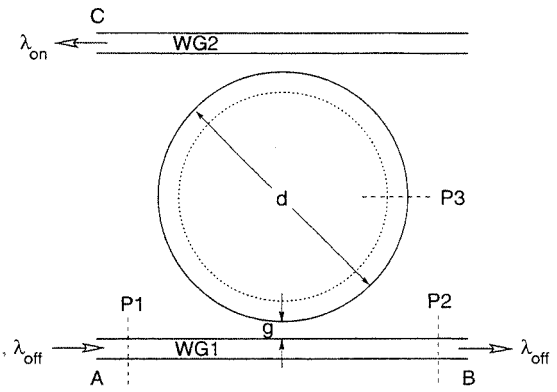

Fig. 1. Schematic of a microcavity ring/disk resonator coupled to two straight waveguides. An off-resonance signal entering port A remains in WG1 and exits at port B; an on-resonance signal is switched to WG2 and exits at port C.

To compute the coupling efficiency, we excite port A of WG1 in its fundamental mode by the wideband Gaussian pulse described in Section II. The coupling coefficient, κ, is defined as the percentage of power coupled into the ring from the input waveguide. The longitudinal power flux passing through a particular waveguide cross-section is obtained as a function of frequency by performing DFT's of the electric and magnetic fields, calculating the Poynting power densities along the cross-section, and summing. The observation cross-sections of interest are at the source end of the input waveguide (P1) and in the ring one-quarter of the way around from the input waveguide (P3). In this manner, a single FDTD simulation provides a complete spectral characterization of κ. Using this method, we have observed power balances (power coupled into the ring as seen at P3 plus power remaining in the waveguide as seen at P2 versus incident power as seen at P1) accurate to four decimal places for cases of negligible scattering loss.

Consider a 5.0-μm-diameter microcavity ring coupled to a straight single-mode input waveguide. Here we focus on the gap between the input waveguide and the microring as the design parameter. Based on current nanofabrication technology, the gap width can be as small as 0.1 μm. Fig. 2 shows the FDTD-computed κ for TM polarization (electric field perpendicular to the plane of the ring) for gap sizes varying from 0.19 to 0.26 μm. Two well-known coupling phenomena are illustrated in this figure. First, at a given frequency, the level of coupling decreases as the gap size increases. Second, for a fixed gap size, the level of coupling decreases at higher frequencies where the effective gap size increases. In order to achieve good transmission characteristics and large extinction ratios, the microcavity resonator coupling efficiency should be greater than the round-trip cavity loss. The desired range for κ is typically 0.5–3%, depending on the propagation loss. Also, the coupling efficiency should be symmetric; that is, the coupling between WG1 and the ring/disk should be equal to the coupling between WG2 and the ring/disk. From Fig. 2, we see that at $\lambda = 1.5\,\mu$m ($\nu = 200$ THz), the percentage of coupling ranges between 0.7 and 2.8%. This is achieved for a change of less than 100 nm in g. Hence, it is feasible to fabricate the small gap size required to achieve the desired range of coupling. However, the FDTD

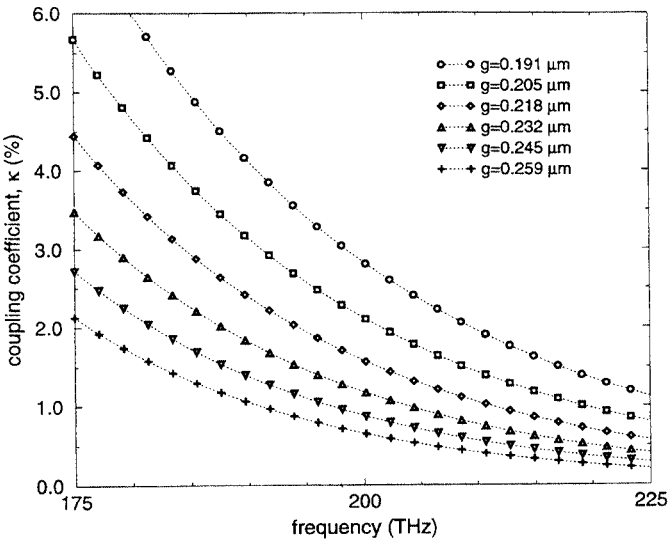

Fig. 2. FDTD-computed coupling coefficients as a function of frequency and gap size, g, for a straight single-mode input waveguide coupled to a 5.0-μm-diameter microcavity ring (TM polarization).

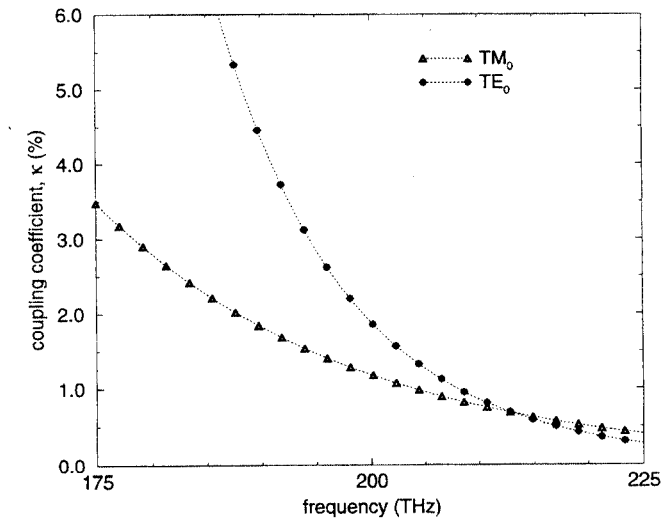

Fig. 3. Comparison between coupling coefficients for TM and TE polarizations. Here, $g = 0.232\,\mu$m, $d = 5.0\,\mu$m, and the waveguide width is 0.3 μm.

simulations indicate that the level of coupling is very sensitive to the size of the gap between the input/output waveguide and the microring resonator. Therefore, since it is difficult to fabricate identical gaps to such high precision, the coupling may be slightly asymmetric in the actual ring or disk.

In Fig. 3, we compare the coupling coefficient curve of Fig. 2 for $g = 0.232\,\mu$m with results computed for the fundamental TE mode (electric field parallel to the plane of the ring) for the same gap size. The TE coupling coefficient at 1.5 μm is 1.9%, compared with 1.2% for the TM case. The TE coupling is greater for most of the spectrum of interest. In order avoid high lateral coupling of light to the media surrounding the waveguides and the ring or disk, relatively wide boundary trenches must be etched (look ahead to Fig. 11). In the present work, the fabricated trenches are 1.0 μm wide. This trench is sufficiently wide to avoid strong coupling of TM light to

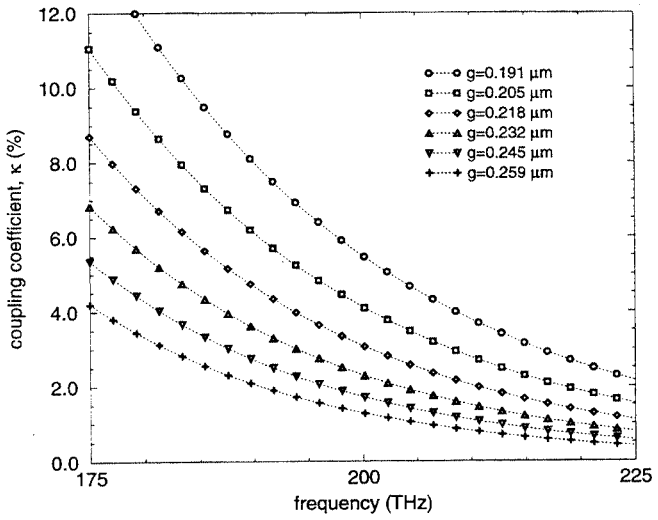

Fig. 4. FDTD-computed coupling coefficients as a function of frequency and gap size, g, for a straight single-mode input waveguide coupled to a 10.0-μm-diameter microcavity ring (TM polarization).

the surrounding media. However, as discussed below in the context of the nanofabrication and experimental results, this trench size was not wide enough for the TE-polarized light. For this reason, we focus on the TM polarization in this paper. We note that with a sufficiently wide trench, the TE polarization case is qualitatively the same as the TM results presented here.

Fig. 4 shows the FDTD results for a 10.0-μm-diameter microring with the same range of gap sizes investigated in Fig. 2. At $\lambda = 1.5\,\mu$m, $1.3\% \leq \kappa \leq 5.5\%$. The 10-$\mu$m-diameter ring resonator has a higher coupling efficiency (by a factor of approximately 2) than the 5-μm-diameter case for a given gap size and frequency. Thus, the interaction length for the larger diameter ring is still short enough to avoid coupling from the ring back to the straight waveguide.

B. Microrings Coupled to Curved Waveguides

In addition to varying the gap size and diameter, the coupling efficiency can be manipulated by adding curvature to the input/output waveguides. As shown in Fig. 5, we consider a waveguide that remains straight from the source plane to the point of smallest separation ($g = 0.205\,\mu$m) from the 5.0-μm-diameter ring. The remaining part of the input waveguide is given a radius of curvature, ρ. For a given value of ρ, the curved part of the input waveguide bends toward the ring for 1/8th of the ring's circumference. The waveguide then bends away from the ring in exactly the same manner. The FDTD-computed coupling coefficients for this waveguide structure are graphed in Fig. 6. The first curve ($\rho = \infty$) is the case of the straight waveguide studied previously. In each additional curve, the bend radius is decreased slightly. The minimum possible value for ρ is $\rho_r + g$, where ρ_r is the radius of the ring; in this extreme, the gap between the ring and waveguide would be constant over a 45° angle. The FDTD simulations show that the coupling drops as the input waveguide bends more toward the ring, suggesting an increasing phase mismatch between the signals in the waveguide and in the ring. We also

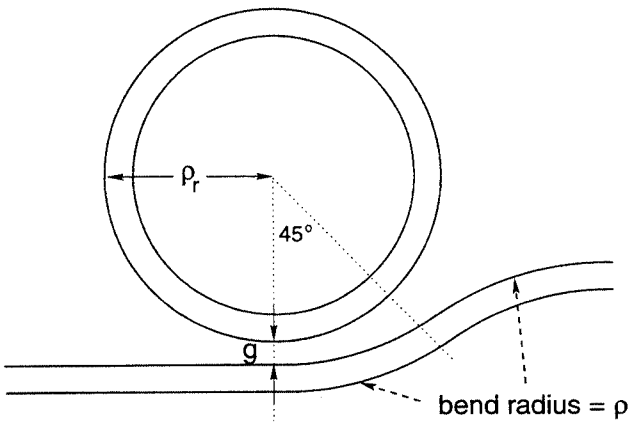

Fig. 5. Schematic of a microcavity ring resonator coupled to a curved waveguide. The bend radius of the waveguide's outer curves is ρ.

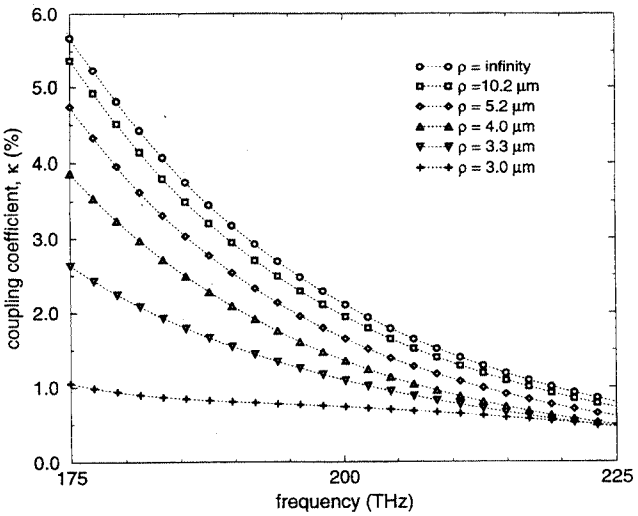

Fig. 6. FDTD-computed coupling coefficients as a function of frequency and input waveguide bend radius, ρ, for the 5.0-μm-diameter microcavity ring resonator ($g = 0.205\,\mu$m).

note that for the smaller values of ρ, the coupling phenomena becomes less sensitive to frequency.

V. Microcavity Ring and Disk Resonances

We now focus on the resonance behavior of the microcavity rings and disks. The channel-dropping/passing nature of the resonators is illustrated in Fig. 1. If the signal that enters port A is on-resonance with the ring or disk, then that signal couples into the cavity from WG1, couples out from the cavity into WG2, and exits the device at port C. A signal that is off-resonance with the cavity remains in WG1 and exits at port B. The output at port B is often called the channel-dropping transmittance; the output at port C is correspondingly called the channel-passing transmittance. The rings and disks support both a clockwise and a counterclockwise propagating mode. By sending a signal into port A, only the counterclockwise propagating mode is directly excited. Backward reflections in the coupling regions and backscattering due to side-wall roughness can excite the counterpropagating mode.

First, we investigate the resonances of a 5.0-μm-diameter microcavity ring and disk resonator, each coupled to two straight waveguides (Fig. 1). For these simulations, the gap between each waveguide and the ring or disk is 0.232-μm-wide and the width of WG1, WG2, and the ring waveguide is 0.3 μm. The spectral responses of the resonators are computed as follows. WG1 is excited in the same way as in the coupling studies. Time-stepping is continued as the pulse initially couples into the resonator and travels around the ring or disk, coupling energy out to the two adjacent waveguides at each pass. This results in a series of output pulses of diminishing amplitude at the output ports of WG1 and WG2. The simulation is run until the energy in the resonator has sufficiently died down. We are assured that the simulated decay of energy is purely physical since the FDTD numerical algorithm is nondissipative. To determine the transmittance at port B, we compute the longitudinal power flux passing through waveguide cross-sections P1 and P2 via the same procedure used for the coupling studies and then form a ratio of the output to input power.

Fig. 7 is a visualization of snapshots in time of the FDTD-computed E-field (perpendicular to the plane) as the pulse first couples into the microring [Fig. 7(a)] or microdisk [Fig. 7(b)] cavity and completes one round trip. For best display dynamic range, the gray scale in each snapshot is normalized to the maximum E-field in that snapshot. In addition to illustrating the simulation procedure, Fig. 7 also illustrates the difference in group velocities between the ring and the disk. In the final panel of Fig. 7(a), the pulse coupled into the ring is just short of completing one round trip after 240 fs. The pulse also maintains its single-mode transverse profile. In Fig. 7(b), the same pulse has a greater group velocity in the disk and therefore has propagated farther around the disk after 240 fs. Here, the pulse in the disk has also broadened and is starting to trace out the whispering-gallery modes.

The transmittance for the microcavity ring is graphed in Fig. 8(a). The Q of the mth resonance is obtained directly from the power spectrum by forming the ratio of the center frequency, ν_m, to the width of the resonance, $\Delta\nu_m$, at the half-power points. The resonant frequencies and Q's calculated from the data in Fig. 8(a) are listed in Table I. Based on only the coupling, which decreases at higher frequencies, the Q should increase with frequency. Such behavior is observed for the first two resonances ($m = 25, 26$), but then the Q drops for the higher-frequency resonances. This drop is due to stronger scattering at higher frequencies, where imperfections in the etched side walls (stepped-edge approximations to the ideally smooth ring) have more of an effect. In fact, on an expanded frequency scale, it is clear that each of the $m = 28$ and $m = 29$ resonances has split into two subresonances. The sidewall roughness has caused backscattering into a counterpropagating mode; this low-intensity counterdirectional coupling splits the resonance peak [46]. If the resulting two subresonances are not split far enough apart to be individually discernable, then the Q of each subresonance cannot be determined and the apparent Q of the overall resonance is lowered. This is the case for the higher-frequency resonances of Fig. 8(a). We have verified the drop in the apparent Q by simulating a

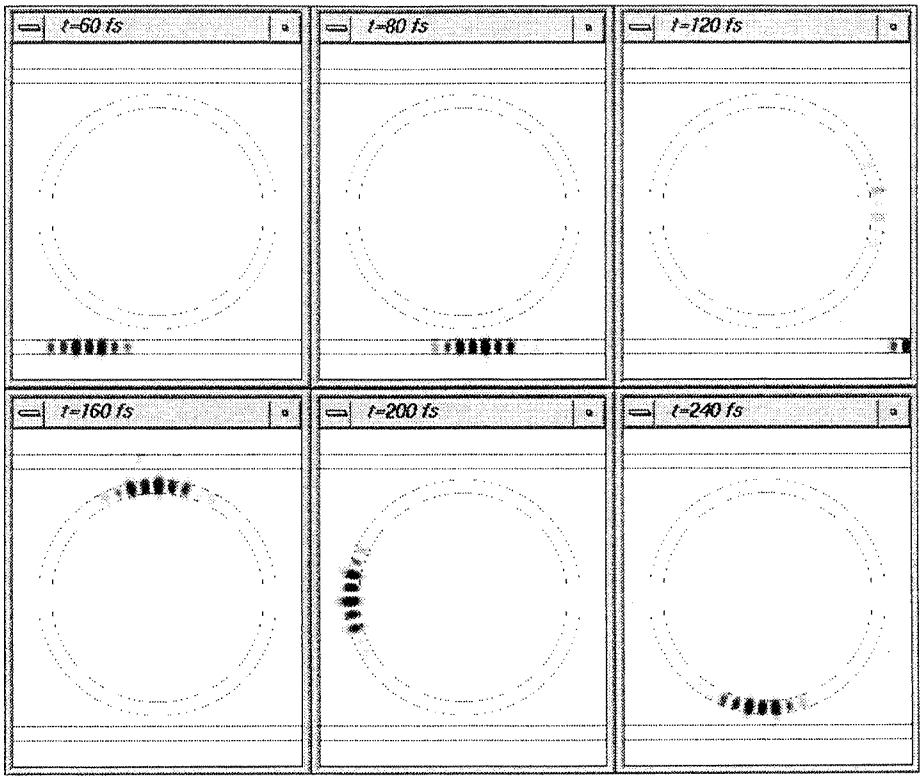

(a)

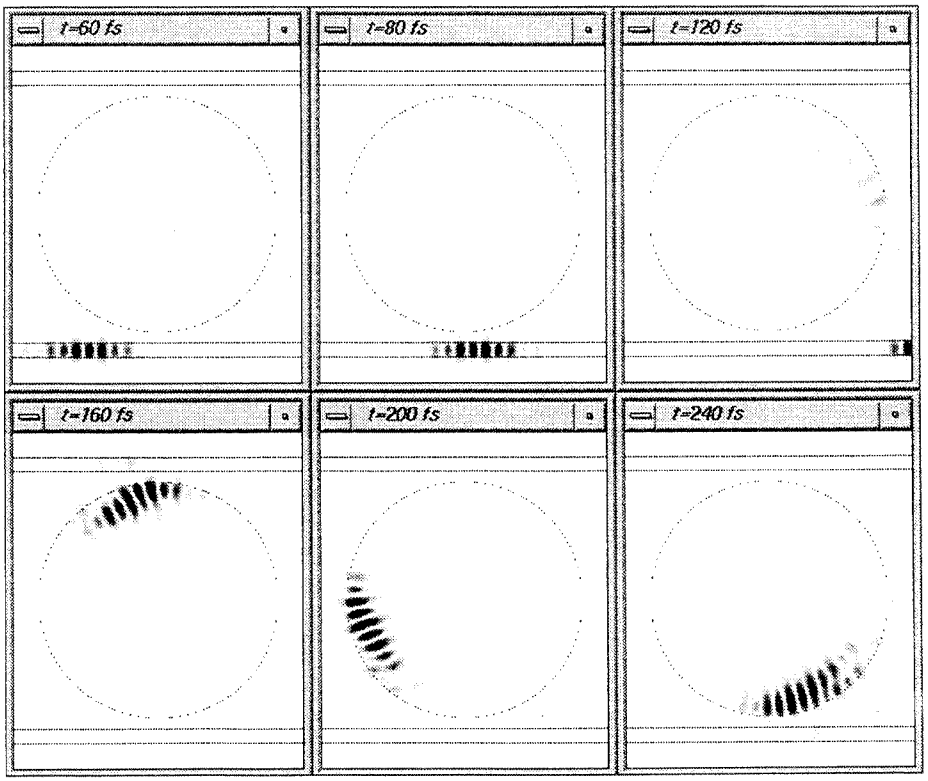

(b)

Fig. 7. Visualization of the FDTD-computed initial coupling and circulation of the exciting 20-fs pulse around the 5.0-μm-diameter microcavity resonators: (a) ring and (b) disk.

microring resonator that has a rougher sidewall (coarser by a factor of 2). In this case, all five resonances are split as a result of higher scattering losses across the 25 THz spectrum. Furthermore, the two highest frequency resonances are split far enough apart to individually resolve each subresonance. We observe an increasing Q with increasing mode number for each

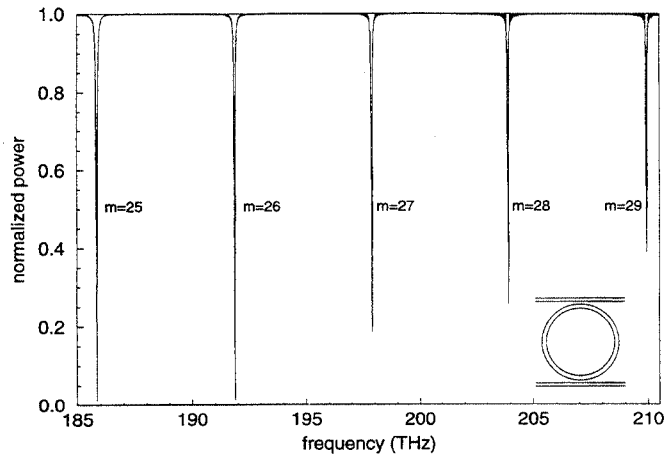

(a)

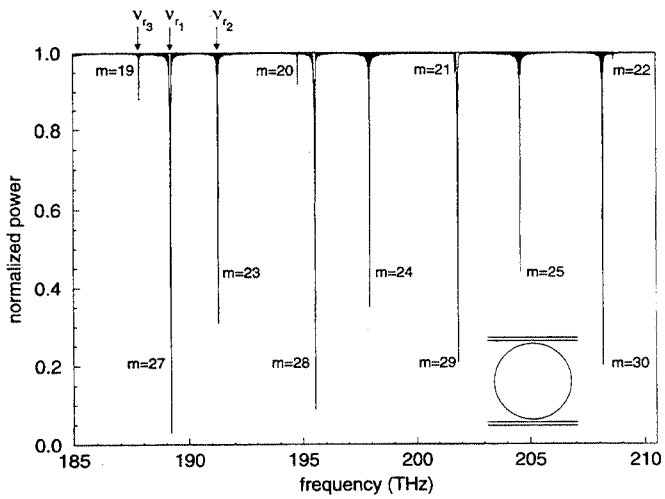

(b)

Fig. 8. FDTD-computed transmittance for the 5.0-μm-diameter microcavity resonators coupled to straight 0.3-μm-wide waveguides: (a) ring and (b) disk.

subresonance, as expected based on the strong dependence of coupling on frequency.

We have also calculated the spacing between resonances. The FSR values listed in Table I decrease as the wavelength decreases. This behavior agrees with our experimental observations and is a consequence of the relatively large waveguide dispersion. The finesse, defined as the ratio of the FSR to the resonance width, ranges between 115 and 160. The 5.0-μm-diameter microcavity ring resonator demonstrates narrow channel wavelength selectivity (high finesse) and constant transmittance over a FSR as wide as 6.026 THz (50.66 nm).

The on/off ratio, or rejection ratio, is defined here as the ratio of power transmitted at a resonance frequency to the power not transmitted at that frequency. Consider the 30-nm communications window of erbium amplifiers that is centered around 1.55 μm. Focusing on this window, that is, around the $m = 26$ resonance in Fig. 8(a), we calculate a rejection ratio of approximately 72 : 1. By slightly decreasing the gap size from the case shown in Fig. 8(a), the rejection ratio can be increased to more than 500 : 1. In general, the rejection ratio can be optimized over any desired band spanning a couple of

TABLE I
RESONANCE DATA FROM FIG. 8(a) FOR THE 5.0-μm-DIAMETER MICROCAVITY RING RESONATOR

m	ν_m (THz)	λ_m (nm)	Q	FSR (nm)
25	185.85	1613.10	3700	
				50.66
26	191.88	1562.44	5000	
				47.56
27	197.90	1514.88	4000	
				44.73
28	203.92	1470.15	4000	
				42.17
29	209.94	1427.98	4000	

THz by adjusting the gap size to change the coupling with respect to the scattering losses in that wavelength range.

Since we know n_{eff} as a function of frequency for the straight waveguides of Section II, we can estimate d_{eff} as $mc/\nu_m n_{\text{eff}}\pi$ for this ring resonator and compare the results with the disk. For the resonances in Fig. 8(a), d_{eff} increases with frequency from 4.717 to 4.720 μm. If the circumferential path of the mode was along the center of the waveguide, d_{eff} would be 4.7 μm (halfway between the outer rim diameter of 5.0 μm and the inner rim diameter of 4.4 μm). We note that our estimate of d_{eff} is slightly larger, agreeing with the expectation that the peak of the transverse mode profile shifts toward the outer edge of the curved waveguide.

In Fig. 8(b), we have graphed the normalized power spectrum for the 5.0-μm-diameter microcavity disk resonator. Note that the disk geometry is identical to that of the 5.0-μm ring except that there is no inner rim. There are three sets of resonances in Fig. 8(b), corresponding to the first- , second- , and third-order radial modes of the disk. As the radial order (the number of electric field intensity maxima in the radial direction) increases, the transmission characteristics worsen. We conclude that while the input waveguide width of 0.3 μm allows coupling into three whispering-gallery modes of the microdisk, the coupling is optimized for the fundamental radial mode. The resonant frequencies, Q's, and FSR's calculated from the data in Fig. 8(b) are listed in Table II. In comparing the first-order radial mode resonance data for the disk with the resonance data for the ring, we note that the locations of the resonances have changed, the FSR values are even wider, and the linewidths are narrower here (the Q's are much higher). We believe that the higher fundamental-mode Q's of the disk resonator, in comparison to the ring, result from the reduced scattering loss arising from the lack of an inner rim. The wider FSR's for the disk arise because the lack of the inner rim allows the effective diameter to be smaller for the fundamental whispering-gallery modes of the disk than for the ring. This phenomena is also evident in comparing the first-order mode FSR's of the disk with the FSR's of the higher-order modes. As the order of the radial mode increases, the peak of the mode moves toward the center of the disk; therefore d_{eff} decreases even further for the higher-order modes. Just as with the microring, the FSR decreases as the wavelength decreases

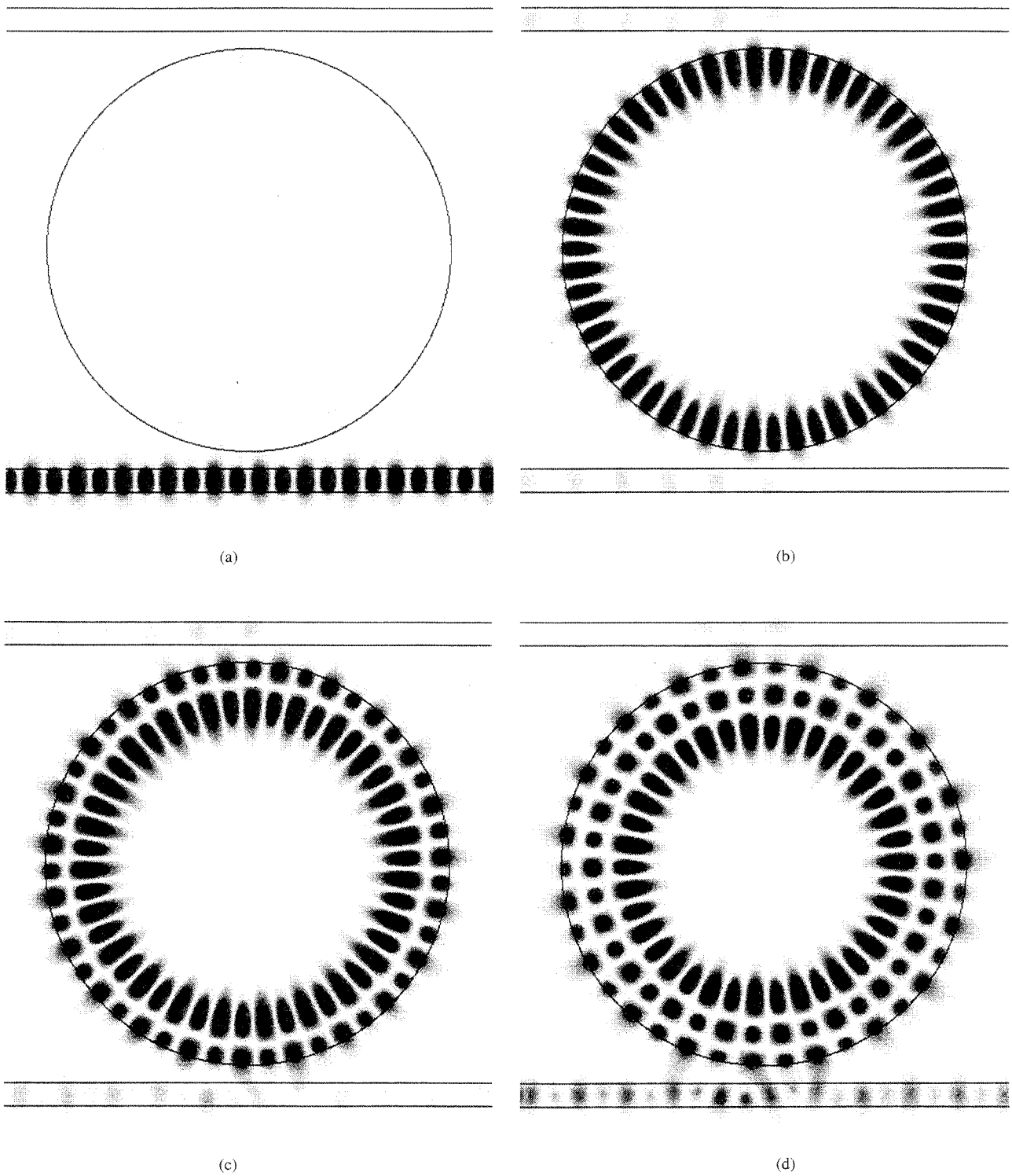

Fig. 9. Visualizations of the FDTD-computed steady-state electric field pattern in a 5.0-μm-diameter microdisk resonator coupled to 0.3-μm-wide waveguides for different single-frequency excitations at port A of WG1. (a) nonresonant signal ($\nu_{nr} = 193.4$ THz), (b) on-resonance signal, first-order radial mode ($\nu_{r_1} = 189.2$ THz), (c) second-order radial mode resonance ($\nu_{r_2} = 191.3$ THz), and (d) third-order radial mode resonance ($\nu_{r_3} = 187.8$ THz).

within a given set of microdisk resonances. In an ideal disk, the low-order modes have the highest Q. But since the lowest-order mode is confined most closely to the perimeter of the disk, it is most sensitive to side-wall roughness. Therefore, as seen in Table II, the higher-order mode resonances have slightly higher Q's because of lower scattering loss.

We have verified the interpretation of the three levels of resonances in Fig. 8(b) by performing single-frequency simulations of the microdisk resonator. Fig. 9(a) shows the steady-state electric field pattern for CW excitation at a non-resonant frequency, $\nu_{nr} = 193.4$ THz (1550.0 nm). From the data graphed in Fig. 8(b) and the steady-state data visualized

TABLE II
RESONANCE DATA FROM FIG. 8(b) FOR THE 5.0-μm-DIAMETER MICROCAVITY DISK RESONATOR. (q = RADIAL ORDER, NA = RESONANCE TOO SMALL TO OBTAIN ACCURATE DATA)

q	m	ν_m (THz)	λ_m (nm)	Q	FSR (nm)
1	27	189.20	1584.51	7600	
					51.32
1	28	195.54	1533.19	7500	
					47.98
1	29	201.85	1485.21	7000	
					45.03
1	30	208.16	1440.18	9100	
2	23	191.29	1567.24	8700	
					52.69
2	24	197.94	1514.55	9900	
					49.12
2	25	204.58	1465.43	11000	
3	19	187.83	1596.10	9900	
					57.09
3	20	194.80	1539.01	9700	
					52.96
3	21	201.74	1486.05	8800	
					(NA)
3	22	~208.65	(NA)	(NA)	

in Fig. 9(a), it can be shown that 99.98% of the power in the incident signal at this frequency remains in WG1. Fig. 9(b) is a visualization for an excitation at $\nu_{r_1} = 189.2$ THz (1584.5 nm), the location of a first-order resonance in Fig. 8(b). The field pattern inside the disk is that of the $m = 27$ first-order radial whispering-gallery mode. Since the gray-scale has been normalized to the peak resonant fields inside the disk, the fields in WG1 and WG2 appear to be very weak; however, they are at the same level as the fields in WG1 in Fig. 9(a). For this on-resonance case, 99.79% of the signal in WG1 has been switched to WG2. In Fig. 9(c), the frequency of excitation is $\nu_{r_2} = 191.3$ THz (1567.2 nm) which corresponds to what we have suggested is a resonant second-order radial mode in Fig. 8(b). This visualization confirms that there are two electric field oscillations in the radial direction, and shows the effect of the peak shifting away from the edge of the disk. Finally, Fig. 9(d) shows the whispering-gallery mode pattern for an excitation at $\nu_{r_3} = 187.8$ THz (1596.1 nm), a third-order radial mode resonance frequency. The visualizations of Fig. 9 illustrate how each resonant mode is confined to an annulus around the perimeter of the disk; the width of the annulus increases as the radial order increases. A comparison between Figs. 9(a) and (b) indicates the potential for high extinction ratios (and low crosstalk between channels) in these devices if the higher-order modes of the microdisk can be suppressed.

To understand the relationship between the whispering-gallery mode resonances of a microdisk and the single-mode resonances of a thin microring, we study three intermediate geometries that bridge the gap between the extremes of the thin ring and solid disk. We perturb only the cavity geometry; the air gap between the 0.3-μm-wide waveguides and microcavity remain constant ($g = 0.232\,\mu$m). Starting with the solid 5.0-μm-diameter microdisk, we etch out the center to form a wide ring with an inner rim diameter d_i of 3.0 μm, thereby yielding a waveguide width, w, of 1.0 μm. The FDTD-computed transmittance for this structure is shown in Fig. 10(a). The first- and second-order whispering-gallery mode resonances remain unchanged from that of the solid disk [see Fig. 8(b)]. The effect of creating an inner ring boundary is to shift the third-order resonances toward higher frequencies and to lower the Q, that is, to begin to suppress the third-order radial mode which has fields concentrated toward the center of the disk. In the next structure, d_i is increased to 3.5 μm so that w = 0.75 μm. Fig. 10(b) shows that the third-order mode resonances have been completely suppressed. Furthermore, each second-order resonance has shifted upward in frequency; only the first-order resonances remain unaffected. In the final structure, which approaches the geometry of the thin microring, the waveguide width of the ring is further reduced to 0.5 μm ($d_i = 4.0\,\mu$m). The transmittance curve shown in Fig. 10(c) reveals further suppression and shifting of the second-order mode resonances. In this case, the fundamental mode resonances are also shifted and the Q's are slightly lowered. We note that the resonance behavior in Fig. 10(c) is approaching that of the single-mode narrow-waveguide microring shown in Fig. 8(a). In summary, as the inner diameter of the microring is increased, each set of resonances is monotonically shifted toward higher frequencies, as seen by tracking the location of specific resonances through Figs. 8(b), 10(a)–(c), and 8(a). These studies demonstrate the transition between the multi-whispering-gallery-mode resonances of the solid microdisk resonator and the single-mode resonances of the 0.3-μm-waveguide microring resonator. Clearly, the size of the inner diameter in a microcavity ring resonator is an important design factor in determining the resonance frequencies and Q's.

VI. NANOFABRICATION AND EXPERIMENTS

We are using nanofabrication techniques to realize these microcavity ring and disk resonators. The scanning electron microscope (SEM) images in Fig. 11 show a 10.5-μm-diameter ring (on the left) and disk (on the right) coupled to two straight 0.5-μm-wide waveguides. The fabricated gap widths are 0.1 μm. The resonator patterns were created on PMMA with electron-beam lithography (JEOL JBX 5DII). Using reactive ion etching, the PMMA mask was transferred to an underlying SiO_2 layer to provide a more durable mask. The AlGaAs/GaAs was then etched using chemically assisted ion-beam etching with chlorine and argon process gases. The resonators and input/output waveguides, as seen in the SEM images, are defined and isolated from the rest of the sample by etching a 1.0-μm-wide trench (the dark regions in the images). The resonators were experimentally characterized by end-firing light from a tunable laser diode into the adjacent waveguides. In our experimental measurements, we observed strong resonances for the TM polarization. In hindsight, the 1.0-μm-wide trench was not sufficient to keep the TE-polarized light from coupling to the surrounding media.

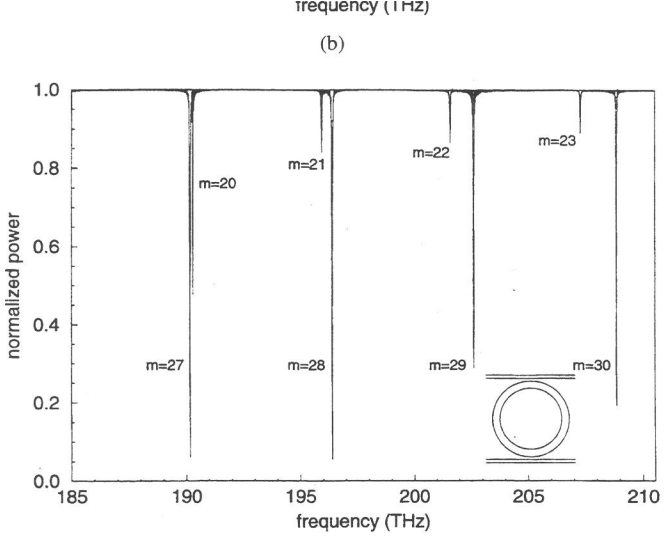

(b)

(c)

Fig. 10. FDTD-computed transmittance of a 5.0-μm-diameter microcavity resonator coupled to 0.3-μm-wide waveguides. The inner rim diameter, d_i, is increased from the case of the solid disk ($d_i = 0$) toward the case of the narrow-waveguide ring ($d_i = 4.4\,\mu$m). (a) $d_i = 3.0\,\mu$m (ring waveguide width, w, is 1.0 μm), (b) $d_i = 3.5\,\mu$m (w = $0.75\,\mu$m), and (c) $d_i = 4.0\,\mu$m (w = $0.5\,\mu$m).

Consequently, we were unable to observe resonances for the TE case because of the resulting higher cavity loss. In future fabrications, the trench can be widened to eliminate this loss mechanism.

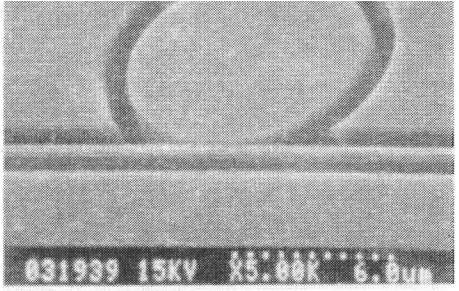

(b).

Fig. 11. SEM images of a 10.5-μm-diameter GaAs/AlGaAs microcavity ring (a) and disk (b) resonator coupled to 0.5-μm-wide waveguides.

In Fig. 12(a), we show the measured transmittance curve for the 10.5-μm-diameter microdisk of Fig. 11. The measured FSR's are 21.2 and 21.6 nm; the larger FSR corresponds to the larger wavelength resonances. In Fig. 12(b), we also plot the FDTD-computed transmittance for the same resonator (dotted line). On the expanded wavelength scale, we see that the linewidths of the experimental and FDTD-computed resonances are less than 0.5 nm. The FDTD simulation reveals that for 0.5-μm-wide waveguides coupled to a 10.5-μm-diameter disk, two sets of whispering-gallery mode resonances are supported. The second-order radial mode resonances in the FDTD transmittance curve are not seen in the experimental data (solid line). It is likely that, since the transmission characteristics of the experimentally measured fundamental-

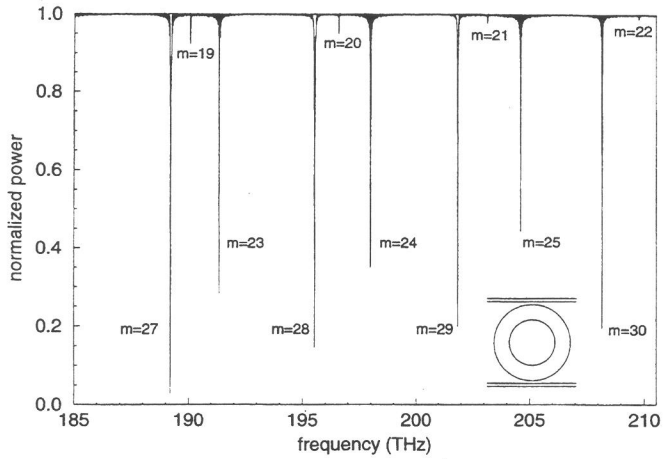

(a)

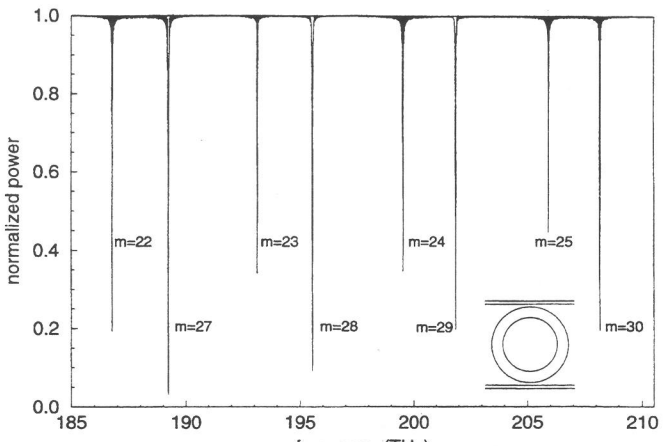

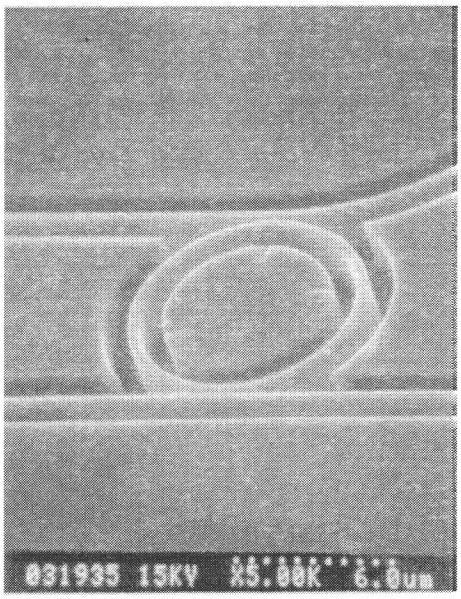

(a)

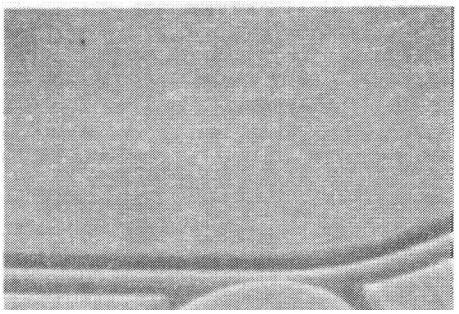

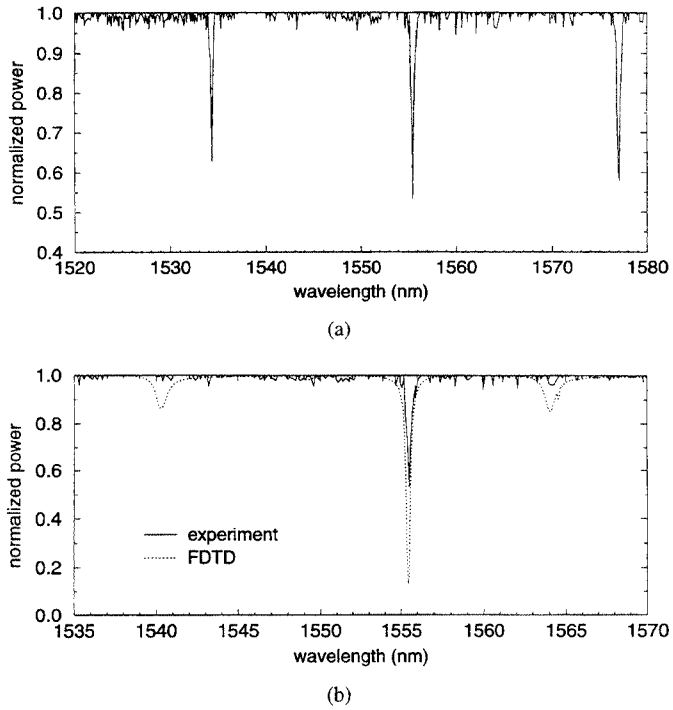

Fig. 12. (a) Measured transmittance of the 10.5-μm-diameter microdisk resonator in Fig. 11. (b) Comparison of the measured (solid line) and the FDTD-computed (dotted line) transmittance curves. The expanded wavelength scale highlights the linewidth agreement of the fundamental mode resonances.

mode resonances show a higher loss than the FDTD-computed resonances, any second-order resonances would also see a higher loss than those in the FDTD results. In this case, the very shallow second-order resonances would be on the order of the Fabry–Perot resonances of the adjacent 3-mm-long input/output waveguide. Therefore, we believe that any evidence of second-order modes in the experiment was lost during the data normalization process required to remove the Fabry-Perot resonances. We attribute the higher loss observed experimentally to the coupling loss across the 1-μm trench to the surrounding media.

VII. Conclusions

In this paper, we have studied the coupling and resonance behavior of high-Q semiconductor microcavity ring and disk resonators coupled to single-mode or nearly single-mode waveguides. Using the FDTD method, we have characterized these devices while taking into account the effects of waveguide curvature, waveguide dispersion, and side-wall roughness. We can achieve FSR's as wide as 6 THz (50 nm) using microcavity diameters of 5.0 μm. Also, we have reported preliminary experimental results from the first demonstration of this type of microresonator which shows the feasibility of realizing this new class of integrated optical devices. Full-wave electromagnetic modeling has been found to be an important element in the design process of this emerging nanoscale device technology. We expect microcavity ring and disk resonators to have wide applications in optical communications and signal processing.

References

[1] K. Oda, S. Suzuki, H. Takahashi, and H. Toba, "An optical FDM distribution experiment using a high finesse waveguide-type double ring resonator," *IEEE Photon. Technol. Lett.*, vol. 6, pp. 1031–1034, Aug. 1994.

[2] R. Orta, P. Savi, R. Tascone, and D. Trinchero, "Synthesis of multiple-ring-resonator filters for optical systems," *IEEE Photon. Technol. Lett.*, vol. 7, pp. 1447–1449, Dec. 1995.

[3] K. Sasayama, F. Früh, T. Kominato, and K. Habara, "Photonic frequency-division-multiplexing highway switch using integrated-optic multiple ring resonators," *IEICE Trans. Commun.*, vol. E78-B, pp. 674–678, May 1995.

[4] W. Weiershausen and R. Zengerle, "Photonic highway switches based on ring resonators used as frequency-selective switches," *Appl. Opt.*, vol. 35, pp. 5967–5978, Oct. 1996.

[5] K. Oda, N. Takato, and H. Toba, "A wide-FSR waveguide double-ring resonator for optical FDM transmission systems," *J. Lightwave Technol.*, vol. 9, pp. 728–736, June 1991.

[6] T. Kominato, Y. Ohmori, N. Takato, H. Okazaki, and M. Yasu, "Ring resonators composed of GeO_2-doped silica waveguide," *J. Lightwave Technol.*, vol. 10, pp. 1781–1787, Dec. 1992.

[7] R. Adar, M. R. Serbin, and V. Mizrahi, "Less than 1 dB per meter propagation loss of silica waveguides measured using a ring resonator," *J. Lightwave Technol.*, vol. 12, pp. 1369–1372, Aug. 1994.

[8] P. Heimala, P. Katila, J. Aarnio, and A. Heinämäki, "Thermally tunable integrated optical ring resonator with poly-Si thermistor," *J. Lightwave Technol.*, vol. 14, pp. 2260–2267, Oct. 1996.

[9] S. Suzuki, K. Oda, and Y. Hibino, "Integrated-optic double-ring resonators with a wide free spectral range of 100 GHz," *J. Lightwave Technol.*, vol. 13, pp. 1766–1771, Aug. 1995.

[10] G. Barbarossa, A. M. Matteo, and M. N. Armenise, "Theoretical analysis of triple-coupler ring-based optical guided-wave resonator," *J. Lightwave Technol.*, vol. 13, pp. 148–157, Feb. 1995.

[11] A. F. Jezierski and P. J. R. Layborn, "Integrated semiconductor ring lasers," *Inst. Elect. Eng. Proc. J.*, vol. 135, pp. 17–24, Feb. 1988.

[12] T. Krauss, P. J. R. Laybourn, and J. Roberts, "CW operation of semiconductor ring lasers," *Electon. Lett.*, vol. 26, pp. 2095–2097, Dec. 1990.

[13] J. P. Hohimer, D. C. Craft, G. R. Hadley, G. A. Vawter, and M. E. Warren, "Single-frequency continuous-wave operation of ring resonator diode lasers," *Appl. Phys. Lett.*, vol. 59, pp. 3360–3362, Dec. 1991.

[14] H. Han, M. E. Favaro, D. V. Forbes, and J. J. Coleman, "$In_xGa_{1-x}As$-$Al_yGa_{1-y}As$-GaAs strained-layer quantum-well heterostructure circular ring lasers," *IEEE Photon. Technol. Lett.*, vol. 4, pp. 817–819, Aug. 1992.

[15] S. L. McCall, A. F. J. Levi, R. E. Slusher, S. J. Pearton, and R. A. Logan, "Whispering-gallery mode microdisk lasers," *Appl. Phys. Lett.*, vol. 60, pp. 289–291, Jan. 1992.

[16] D. Y. Chu, M. K. Chin, N. J. Sauer, Z. Xu, T. Y. Chang, and S. T. Ho, "1.5-μm InGaAs/InAlGaAs quantum-well microdisk lasers," *IEEE Photon. Technol. Lett.*, vol. 5, pp. 1353–1355, Dec. 1993.

[17] M. Hovinen, J. Ding, A. V. Nurmikko, D. C. Grillo, J. Han, L. He, and R. L. Gunshor, "Blue-green laser emission from ZnSe quantum well microresonators," *Appl. Phys. Lett.*, vol. 63, pp. 3128–3130, Dec. 1993.

[18] U. Mohideen, W. S. Hobson, S. J. Pearton, F. Ren, and R. E. Slusher, "GaAs/AlGaAs microdisk lasers," *Appl. Phys. Lett.*, vol. 64, pp. 1911–1913, Apr. 1994.

[19] N. C. Frateschi, A. P. Kanjamala, A. F. J. Levi, and T. Tanbun-Ek, "Polarization of lasing emission in microdisk laser diodes," *Appl. Phys. Lett.*, vol. 66, pp. 1859–1861, Apr. 1995.

[20] B. Corbett, J. Justice, L. Considine, S. Walsh, and W. M. Kelly, "Low-threshold lasing in novel microdisk geometries," *IEEE Photon. Technol. Lett.*, vol. 8, pp. 855–857, July 1996.

[21] A. F. J. Levi, R. E. Slusher, S. L. McCall, J. L. Glass, S. J. Pearton, and R. A. Logan, "Directional light coupling from microdisk lasers," *Appl. Phys. Lett.*, vol. 62, pp. 561–563, Feb. 1993.

[22] D. Y. Chu, M. K. Chin, W. G. Bi, H. Q. Hou, C. W. Tu, and S. T. Ho, "Double-disk structure for output coupling in microdisk lasers," *Appl. Phys. Lett.*, vol. 65, pp. 3167–3169, Dec. 1994.

[23] S. C. Hagness, D. Rafizadeh, S. T. Ho, and A. Taflove, "FD-TD computational electromagnetics simulations of microring and microdisk lasers," in *Opt. Soc. Amer. Annu. Meet.*, Rochester, NY, paper ThZ4, Oct. 1996.

[24] D. Rafizadeh, J. P. Zhang, L. Wang, S. C. Hagness, A. Taflove, S. T. Ho, and R. C. Tiberio, "Semiconductor microcavity resonator multiplexer/demultiplexer," in *Opt. Soc. Amer. Annu. Meet.*, Rochester, NY, paper ThP4, Oct. 1996.

[25] E. A. J. Marcatili, "Bends in optical dielectric guides," *Bell Syst. Tech. J.*, vol. 48, pp. 2103–2132, Sept. 1969.
[26] J. P. Zhang, D. Y. Chu, S. L. Wu, W. G. Bi, R. C. Tiberio, C. W. Tu, and S. T. Ho, "Directional light output from photonic-wire microcavity semiconductor lasers," *IEEE Photon. Technol. Lett.*, vol. 8, pp. 968–970, Aug. 1996.
[27] B. E. Little, S. T. Chu, and H. A. Haus, "Micro-ring resonator channel dropping filters," in *IEEE LEOS 8th Annu. Meet.*, San Francisco, CA, Oct. 1995, vol. 2, pp. 233–234.
[28] D. R. Rowland and J. D. Love, "Evanescent wave coupling of whispering gallery modes of a dielectric cylinder," *Inst. Elect. Eng. Proc. J.*, vol. 140, pp. 177–188, June 1993.
[29] T. Yamamoto and M. Koshiba, "Analysis of propagation characteristics of whispering gallery modes in a dielectric disk or a curved rectangular dielectric waveguides," *J. Lightwave Technol.*, vol. 11, pp. 400–404, Mar. 1993.
[30] M. Rivera, "A finite difference BPM analysis of bent dielectric waveguides," *J. Lightwave Technol.*, vol. 13, pp. 233–238, Feb. 1995.
[31] S. Kim and A. Gopinath, "Vector analysis of optical dielectric waveguide bends using finite-difference method," *J. Lightwave Technol.*, vol. 14, pp. 2085–2092, Sept. 1996.
[32] Y. Tomabechi, J. Hwang, and K. Matsumura, "Resonance characteristics on a dielectric disk resonator coupled with a straight waveguide," *Radio Sci.*, vol. 31, no. 6, pp. 1809–1814, 1996.
[33] N. C. Frateschi and A. F. J. Levi, "Resonant modes and laser spectrum of microdisk lasers," *Appl. Phys. Lett.*, vol. 66, pp. 2932–2934, May 1995.
[34] M. K. Chin, D. Y. Chu, and S. T. Ho, "Approximate solution of the whispering gallery modes and estimation of the spontaneous emission coupling factor for microdisk lasers," *Opt. Commun.*, vol. 109, pp. 467–471, July 1994.
[35] K. S. Yee, "Numerical solution of initial boundary value problems involving Maxwell's equations in isotropic media," *IEEE Trans. Antennas Propagat.*, vol. AP-14, pp. 302–307, May 1966.
[36] A. Taflove, *Computational Electrodynamics: The Finite-Difference Time-Domain Method.* Norwood, MA: Artech House, 1995.
[37] R. J. Hawkins, N. K. Madsen, J. S. Kallman, M. D. Feit, C. C. Shang, B. W. Shore, and J. F. DeFord, "Full-wave simulation of the thumbtack laser," in *Integrated Photon. Res. Tech. Dig., 1993*, Palm Springs, CA, vol. 10, pp. 116–119, Mar. 1993.
[38] B. J. Li and P. L. Liu, "Numerical analysis of the whispering gallery modes by the finite-difference time-domain method," *IEEE J. Quantum Electron.*, vol. 32, pp. 1583–1587, Sept. 1996.
[39] B. E. Little and S. T. Chu, "Estimating surface-roughness loss and output coupling in microdisk resonators," *Opt. Lett.*, vol. 21, pp. 1390–1392, Sept. 1996.
[40] S.-T. Chu and S. K. Chaudhuri, "A finite-difference time-domain method for the design and analysis of guided-wave optical structures," *J. Lightwave Technol.*, vol. 7, pp. 2033–2038, Dec. 1989.
[41] J.-P. Berenger, "A perfectly matched layer for the absorption of electromagnetics waves," *J. Comput. Phys.*, vol. 114, pp. 185–200, Oct. 1994.
[42] D. S. Katz, E. T. Thiele, and A. Taflove, "Validation and extension to three dimensions of the Berenger PML absorbing boundary condition for FD-TD meshes," *IEEE Microwave Guided Wave Lett.*, vol. 4, pp. 268–270, Aug. 1994.
[43] J. Yamauchi, M. Mita, S. Aoki, and H. Nakano, "Analysis of antireflection coatings using the FD-TD method with the PML absorbing boundary condition," *IEEE Photon. Technol. Lett.*, vol. 8, pp. 239–241, Feb. 1996.
[44] C. E. Reuter, R. M. Joseph, E. T. Thiele, D. S. Katz, and A. Taflove, "Ultrawideband absorbing boundary condition for termination of waveguiding structures in FD-TD simulations," *IEEE Microwave Guided Wave Lett.*, vol. 4, pp. 344–346, Oct. 1994.
[45] H. Kogelnik and V. Ramaswamy, "Scaling rules for thin-film optical waveguides," *Appl. Opt.*, vol. 13, pp. 1857–1862, Aug. 1974.
[46] B. E. Little, J.-P. Laine, and S. T. Chu, "Surface-roughness-induced contradirectional coupling in ring and disk resonators," *Opt. Lett.*, vol. 22, pp. 4–6, Jan. 1997.
[47] R. E. Slusher, A. F. J. Levi, U. Mohideen, S. L. McCall, S. J. Pearton, and R. A. Logan, "Threshold characteristics of semiconductor microdisk lasers," *Appl. Phys. Lett.*, vol. 63, pp. 1310–1312, Sept. 1993.

S. C. Hagness (S'91) was born in Terre Haute, IN, on December 16, 1970. She received the B.S. degree with highest honors in electrical engineering from Northwestern University, Evanston, IL, in 1993. She is currently completing the Ph.D. degree in electrical engineering at Northwestern University.

Her research interests include computational electromagnetics and integrated photonic devices and circuits.

Ms. Hagness was the recipient of the Eta Kappa Nu Norman R. Carson Award as the Outstanding Junior Electrical Engineering Student in the U.S. in 1992. From 1993 to 1996, she was a National Science Foundation Graduate Fellow. In 1997, she was awarded a Northwestern University Cabell Dissertation-Year Fellowship. is a member of Tau Beta Pi and Eta Kappa Nu.

D. Rafizadeh (S'96) was born in Boston, MA, on August 14, 1969. She received the B.S. degree in electrical engineering from the Massachusetts Institute of Technology, Cambridge, in 1991 and the M.S. degree in electrical engineering from Northwestern University, Evanston, IL, in 1994. She is currently completing the Ph.D. degree in electrical engineering at Northwestern University and will be joining the technical staff at Aerospace Corporation, El Segundo, CA in November 1997.

In the summer of 1993, she was an intern in Lightwave Systems Research at AT&T Bell Laboratories, Crawford Hill, Holmdel, NJ. Her research interests include optical communications, integrated optics, microcavity resonator devices, and nanofabrication.

S. T. Ho (S'83–M'89) received the B.S., M.S., and Ph.D. degrees in electrical engineering from the Massachusetts Institute of Technology, Cambridge, in 1984 and 1989, respectively.

From 1989 to 1991, he was a Member of Technical Staff at AT&T Bell Laboratories, Murray Hill, NJ. Since 1991, he has been a Faculty member in the Department of Electrical and Computer Engineering at Northwestern University, Evanston, IL. His research areas include microcavity lasers, quantum phenomena in low-dimensional photonic structures, nanofabrication, ultrafast nonlinear optical phenomena, optical communications, and quantum optics.

Dr. Ho is a member of Phi Beta Kappa, Tau Beta Pi, Sigma Pi Sigma, and Sigma Xi.

A. Taflove (F'90) was born in Chicago, IL, on June 14, 1949. He received the B.S., M.S., and Ph.D. degrees in electrical engineering from Northwestern University, Evanston, IL, in 1971, 1972, and 1975, respectively.

Since 1988, he has been a Professor in the Department of Electrical and Computer Engineering at Northwestern. He was named an IEEE Fellow for "contributions to the development of the finite-difference time-domain solution of Maxwell's equations," and was a national lecturer for the IEEE Antennas and Propagation Society in 1990–1991. In 1995, he authored the book, *Computational Electrodynamics: The Finite-Difference Time-Domain Method.* His current research interests include FDTD modeling of micron-scale integrated optical devices and circuits.